UC Davis
UC Davis Electronic Theses and Dissertations

Title

Reconstitution and characterization of the Pisum sativum strigolactone signaling pathway

Permalink

Author

Caso, Tara

Publication Date

2021

Peer reviewed|Thesis/dissertation

Reconstitution and characterization of the *Pisum sativum* strigolactone signaling pathway

By

TARA CASO
THESIS

Submitted in partial satisfaction of the requirements for the degree of

MASTER OF SCIENCE

in

Plant Biology

in the

OFFICE OF GRADUATE STUDIES

of the

UNIVERSITY OF CALIFORNIA

DAVIS

Approved:

_____
Nitzan Shabek, Chair

_____
Savithramma P. Dinesh-Kumar

_____
Philipp Zerbe

Committee in Charge

2021

i

Abstract

Strigolactones (SLs) are a recently discovered class of endogenous plant hormones that regulate many integral traits such as leaf senescence and root elongation while also functioning as exuded signaling molecules. In pea (*Pisum sativum*), key players of this hormone pathway include RMS3 (an α/β-fold hydrolase) and *Ps*MAX2 (the F-box component of an SCF E3 ubiquitin ligase module) that coordinate SL-dependent degradation of transcriptional repressors. Strikingly, RMS3 functions as both the SL receptor and an active serine hydrolase that hydrolyzes SLs after they are perceived. This characteristic has raised the questions of whether SL hydrolysis or its mere perception is required for signal propagation, and how exactly the coordination of *Ps*MAX2-RMS3 is related to SL hydrolysis. Here, we elucidate the first crystal structure of RMS3, investigate its enzymatic function by generating two catalytic mutants, and study their effects in SL signaling *in vitro*. The data uncovered in this work hold the potential to broadly impact research into SL perception and signaling in legumes and beyond.

Introduction

The importance of plants to society and human health cannot be overstated, nor can the threat that climate change poses to our current way of life and the vitality of the ecosystems we inhabit. Humanity relies on plants for fibers, oils, food, medicinal compounds, the air we breathe, and much more. To prepare for the coming challenges posed to global health by climate change, it is necessary to broaden our understanding of how vital plant processes are regulated.

A major direction of plant biology research is in pursuit of understanding how plant physiology is regulated at the biochemical level. One particularly key area of interest is the relationship between the plant ubiquitin proteasome system (UPS)—by which proteins (such as transcriptional regulators) are targeted for degradation—and plant hormone signaling pathways.[1,2,3] A notable example of the UPS' involvement in the regulation of plant physiology is its role in the strigolactone (SL) signaling pathway.[1,4] SLs are the most recently characterized class of plant hormones, having been originally discovered as root exudates of cotton that acted as germination stimulants for parasitic plants such as *Striga.*[5] Since then, SLs have been demonstrated to not only act as important signals in both symbiotic and parasitic plant interactions[6] but to affect a variety of plant physiological processes,[7] such as leaf development,[8,9] stem elongation,[10] shoot branching,[11,12,13] lateral root growth,[14] drought responses,[15,16] and nitrogen metabolism.[17,18] The growing recognition of SLs as critical plant hormones has led to a rapidly developing field of study, particularly at the biochemical level.

Natural SLs are terpenoids and share the basic structure of a tricyclic lactone (denoted as the ABC ring) connected to a butenolide group (known as the D ring) *via* an enol ether

bridge (**Fig. 1**).[19,20,21] The CD structure and linkage is conserved and essential for hormonal bioactivity[13]; in contrast, changes to the A and B rings are tolerable,[22] and separate ABC and D rings have been shown to be inactive in plants.[23]
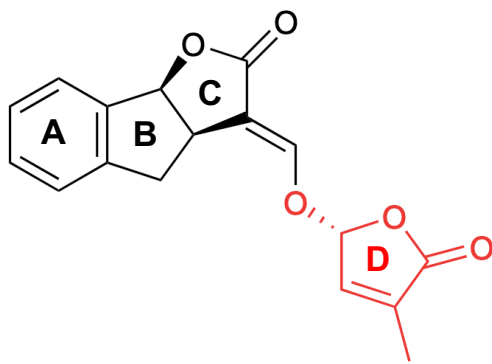

Figure 1: (+)-GR24, an example of an SL. Adapted from de Saint Germain 2013.[22]

The perception and signaling pathway of SLs are coordinated by a handful of highly conserved components. DWARF3 (D3) in rice (orthologous to MAX2 in *Arabidopsis*) is an F-box protein that functions in UPS-mediated proteolysis by binding *Arabidopsis* SKP1-like protein (ASK1) to then function as an interchangeable substrate receptor of an SKP1-CUL1-F-box (SCF) E3 ubiquitin ligase module.[25,26] D14 (denoted as *At*D14 in *Arabidopsis*) is the SL receptor.[23,26,27] D53 (homologous to SMXL6, SMXL7, and SMXL8 in *Arabidopsis*) functions as a transcriptional repressor[28,29] and is ubiquitinated by D3 when bound to D14 in the presence of SLs. D53/SMXLs are consequently degraded by the proteasome, thus mediating developmental processes such as shoot branching.[28,29]

All SL receptors (including rice D14, *At*D14, and the orthologous *Pisum sativum* (pea) RAMOSUS3 (RMS3)) belong to the α/β-fold hydrolase superfamily and contain the Ser, His, and Asp catalytic triad situated in the bottom of a hydrophobic pocket.[30] Binding of the synthetic SL analog GR24 has been shown to involve pocket residues of D14,

presumably through hydrogen bonds and hydrophobic interactions.[13,23,30] After binding, GR24 is hydrolyzed by D14 to yield separate inactive ABC and D ring products.[13,23] There has been much work dedicated to the interaction between D14 and SLs; however, the exact role of SL receptors in SL signaling is still not fully known. It has been suggested that binding and hydrolysis of the SL might trigger a conformational change of the receptor, thus promoting recruitment of D3/MAX2 and initiation of the signaling complex.[7,31,32,33] However, several facets of the receptor's specific role in signaling are unclear, such as whether binding of the SL alone is sufficient for perpetuation of the signal or if hydrolysis is necessary, as well as which conformation of D14 is capable of perceiving SLs (**Fig. 2a**). Early structural studies of strigolactone perception focused on the binding of the hormone to D14 orthologs in isolation.[13,30,34,35,36] Crystal structures of D14s revealed a large, ligand-binding pocket exposed to solvent[23]; thus, SLs were thought to be perceived by D14 and its orthologs in an open conformation, although other conformations during perception have also been suggested.[31,33] A study of the pea D14 ortholog RMS3 suggested that it is a single-turnover enzyme, which produces a covalent D-ring-enzyme complex via the catalytic histidine-247 after substrate hydrolysis and the rapid release of the ABC ring.[22] A crystal structure of rice ASK1–D3 in complex with *At*D14 further uncovered a closed conformation of D3-bound *At*D14, which sequesters the covalently linked intermediate molecule (CLIM) of SL inside an enclosed pocket.[33] These results raised the possibility that the CLIM might represent the active form of the hormone, but this notion is complicated by the identification of several strigolactone agonists that are non-hydrolyzable.[37]
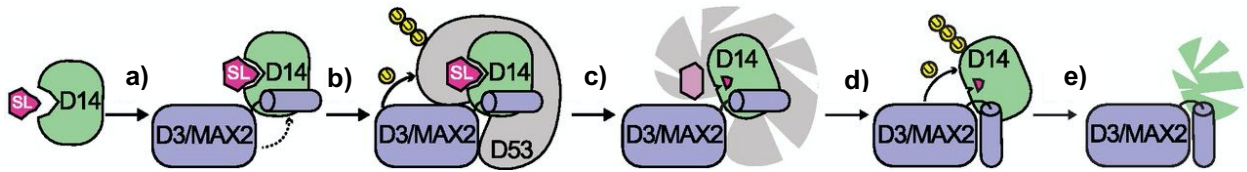
Figure 2: The strigolactone signaling pathway, from binding of SL to receptor to **a)** recruitment of the F-box E3 ligase, **b)** recruitment, ubiquitination, and **c)** degradation of transcriptional repressors, **d)** ubiquitination and finally **e)** degradation of the receptor. Adapted from Tal et al. 2020[1].

In this thesis, we investigated the signaling mechanism of RMS3, the pea ortholog of D14. Historically, legumes such as *P. sativum* have not been the target of thorough structural and biochemical studies, despite being of great interest with regards to SL signaling due to their utilization of SLs in the formation of symbiotic relationships with arbuscular mycorrhizal fungi. Here we performed structure-function investigations of RMS3 and took the first steps in the SL field to elucidate the interactions of RMS3 with the *P. sativum* ortholog of MAX2 (hereon denoted as *Ps*MAX2). We purified and solved the structure of RMS3, characterized its enzymatic function towards a fluorescent SL agonist, and highlighted key structural differences between RMS3 and other D14 orthologs across several important plant families. Additionally, we demonstrated that—like other SL receptors—RMS3 and *Ps*MAX2 co-complex in the presence of SLs. Lastly, we investigated the hormone signaling mechanism of RMS3 by selectively mutating residues within the catalytic triad in an attempt to affect hydrolysis of SLs and binding of *Ps*MAX2. The data gathered in this study provide an important layer of understanding of SL perception and signaling in legumes, and the knowledge gained from this investigation holds promise with regards to future synthetic biology applications of SLs to improve crops and food security globally.

Results and Discussion

Cloning and expression test of His-SUMO-RMS3

RMS3 was cloned and expressed as a 6xHis-SUMO fusion protein from the pAL expression vector and transformed into *E. coli*. A small-scale expression test was then performed to ensure proper expression of the target protein at the correct size, visualized by Coomassie Blue stain (**Fig. 3**).
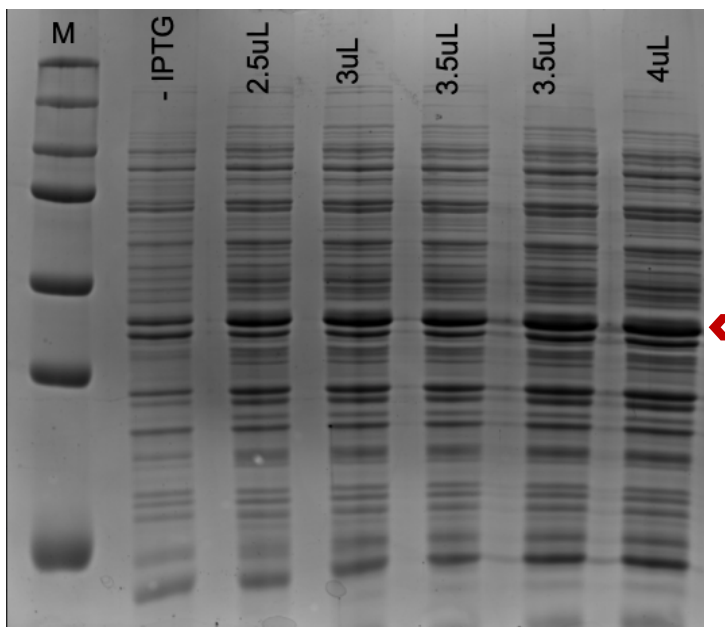

Figure 3: SDS-PAGE depicting an expression test for RMS3, showing enrichment of the target protein post-induction of expression via IPTG. The amount of post-induction sample added to the well is denoted above each lane. M = size marker.

Protein purification of RMS3

After sufficient expression of His-SUMO-RMS3 was verified, the growth conditions were upscaled. The cells of *E. coli* were harvested by centrifugation, lysed, and centrifuged further to separate free, soluble His-SUMO-RMS3 from the other cellular contents. The

His-SUMO-RMS3 was clarified from the supernatant via washing with buffers and affinity chromatography (**Fig. 4b**), then further purified via anion exchange chromatography (**Fig. 4c**). The elution fractions were analyzed via sodium dodecyl sulfate-polyacrylamide gel electrophoresis (SDS-PAGE) and concentrated to greater than 6mg/mL. Tobacco etch virus (TEV) protease was added and the protein solution was incubated at 4°C overnight to cleave off the His-SUMO tag. From there, the solution underwent affinity chromatography once more to purify successfully cleaved RMS3 from remaining His-SUMO-RMS3 and excess His-SUMO tag (**Fig. 4d**). Prior to all biochemical assays and crystallization trials, the cleaved RMS3 was subjected to size-exclusion chromatography (SEC) (**Fig. 4e**).

Verification of RMS3 activity via DSF

Biochemical activity of purified RMS3 was verified via differential scanning fluorimetry (DSF)[32,38] by comparing protein melting temperatures (T_m) with or without the addition of racemic GR24 ((±)-GR24), a synthetic strigolactone. A decrease in T_m is generally interpreted as a decrease in protein stability, and an increase in T_m is interpreted as an increase in stability.[38]

Without (±)-GR24, RMS3 was shown to have a standard T_m of ~45.5°C whereas the addition of 300µM (±)-GR24 decreased the T_m to approximately 40°C (**Fig. 5a**), which is consistent with previous work.[32] To further confirm the biochemical activity of RMS3 in accordance with what has been previously shown, the DSF experiments were repeated using a gradient of (±)-GR24 (**Fig. 5b**).
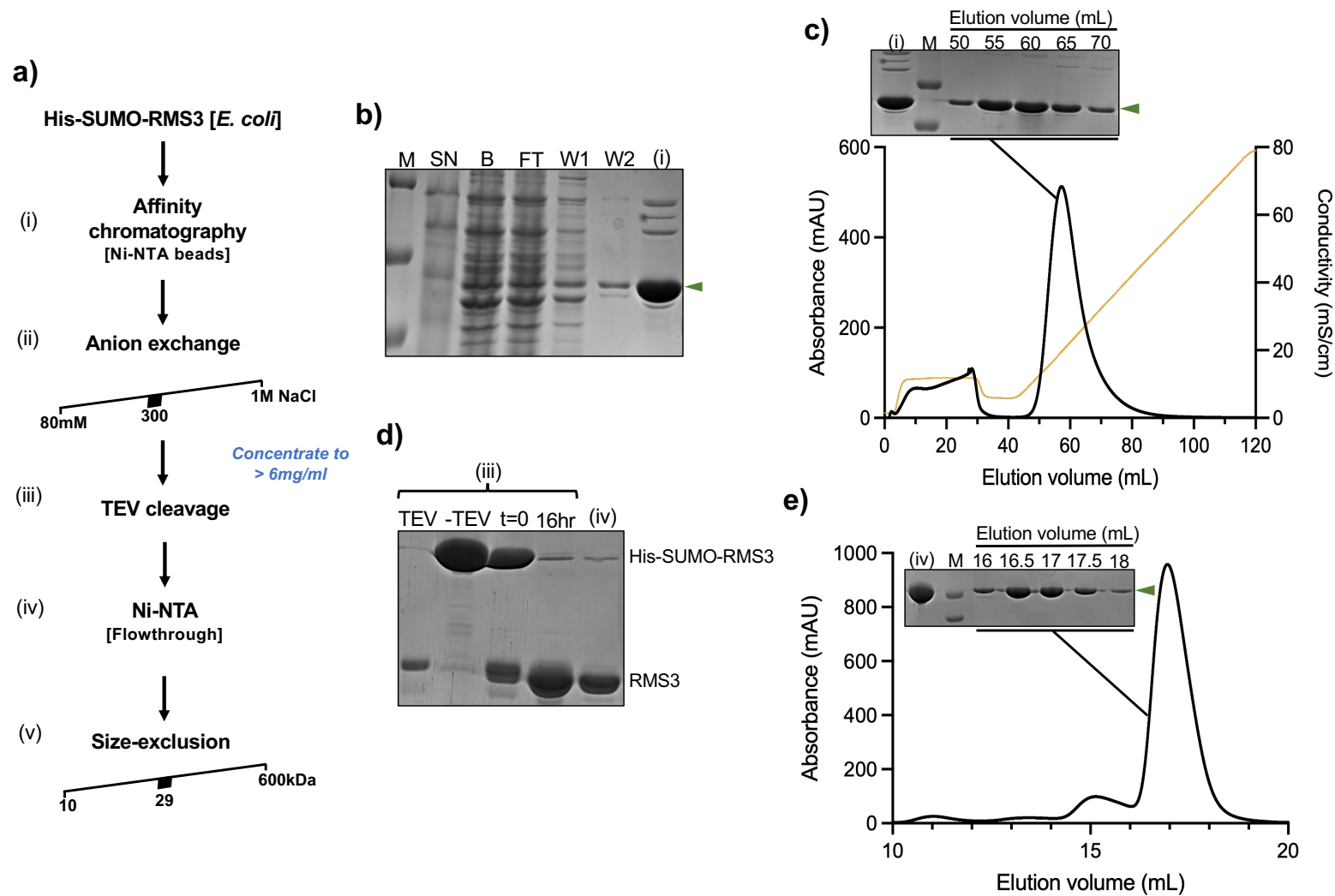
Figure 4: Purification of RMS3. **a)** The purification of RMS3 laid out step by step, from expression in *E. coli* to tag cleavage and purification via size-exclusion chromatography. **b)** and **d)** Sodium dodecyl-sulfate polyacrylamide gels depicting different steps of the purification. M = marker, SN = supernatant, B = beads post-binding, FT = flowthrough, W1 and W2 = wash 1 and wash 2 respectively. TEV = tobacco etch virus. **c)** Anion exchange chromatography of His-SUMO-RMS3 and **e)** size-exclusion chromatography of RMS3, with sodium dodecyl sulfate-polyacrylamide gel electrophoresis analysis of the elution fractions.

A noticeable shift in T_m was observed at concentrations of (±)-GR24 equal to or greater than 100μM, which is comparable to previous DSF assays of RMS3.[32] Thus, we concluded that our purified RMS3 was a functional SL receptor.
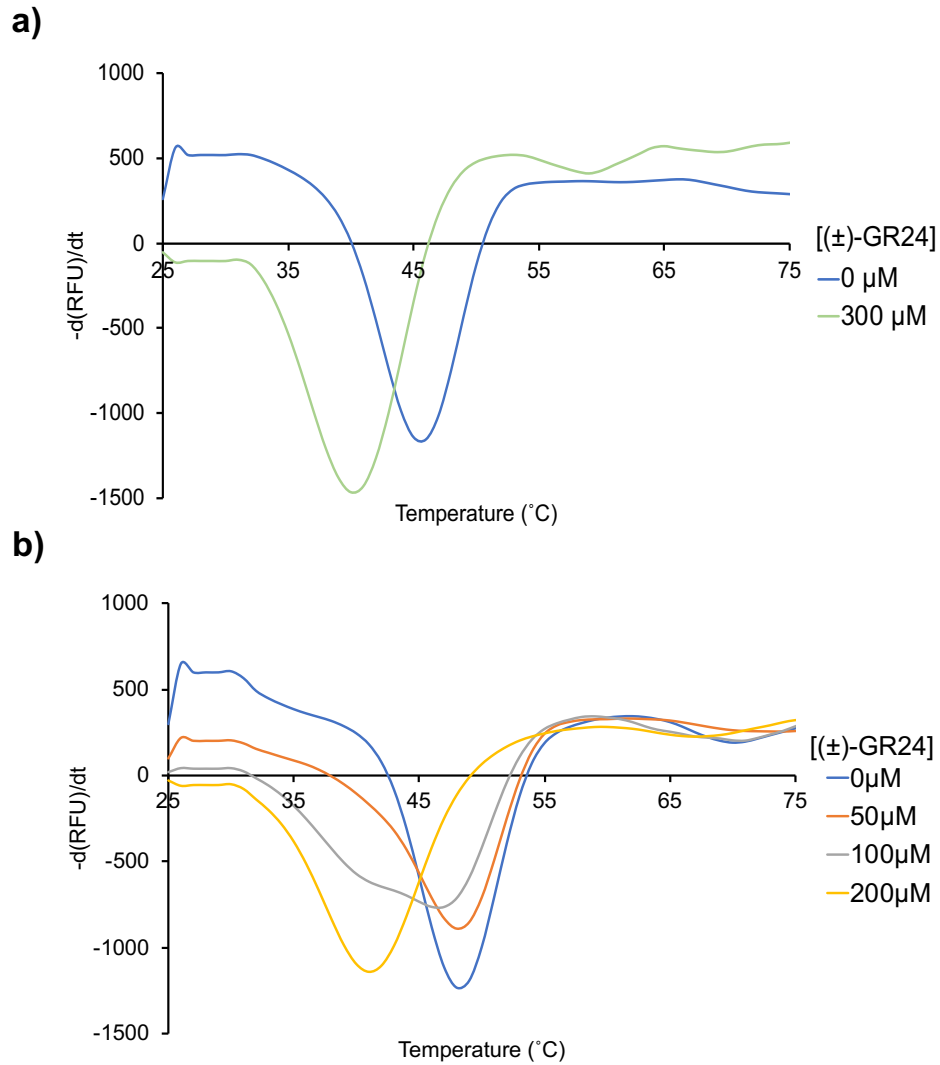
a)

b)

Figure 5: Melting temperature curves for RMS3 at indicated concentrations of (±)-GR24, as assessed by DSF. Each line represents the average protein melt curve for three replicate samples run in parallel.

Analysis of RMS3 hydrolytic activity via YLG hydrolysis

Rice D14 was previously shown to hydrolyze the fluorogenic strigolactone agonist Yoshimulactone Green (YLG).[31] To test its hydrolytic activity, RMS3 was held at constant concentration and subjected to a gradient of YLG (**Fig. 6a**). The data were used to assess the Michaelis-Menten constant (K_m), k_{cat}, and catalytic efficiency (k_{cat}/K_m) toward YLG as well (**Fig. 6b** and **c**).
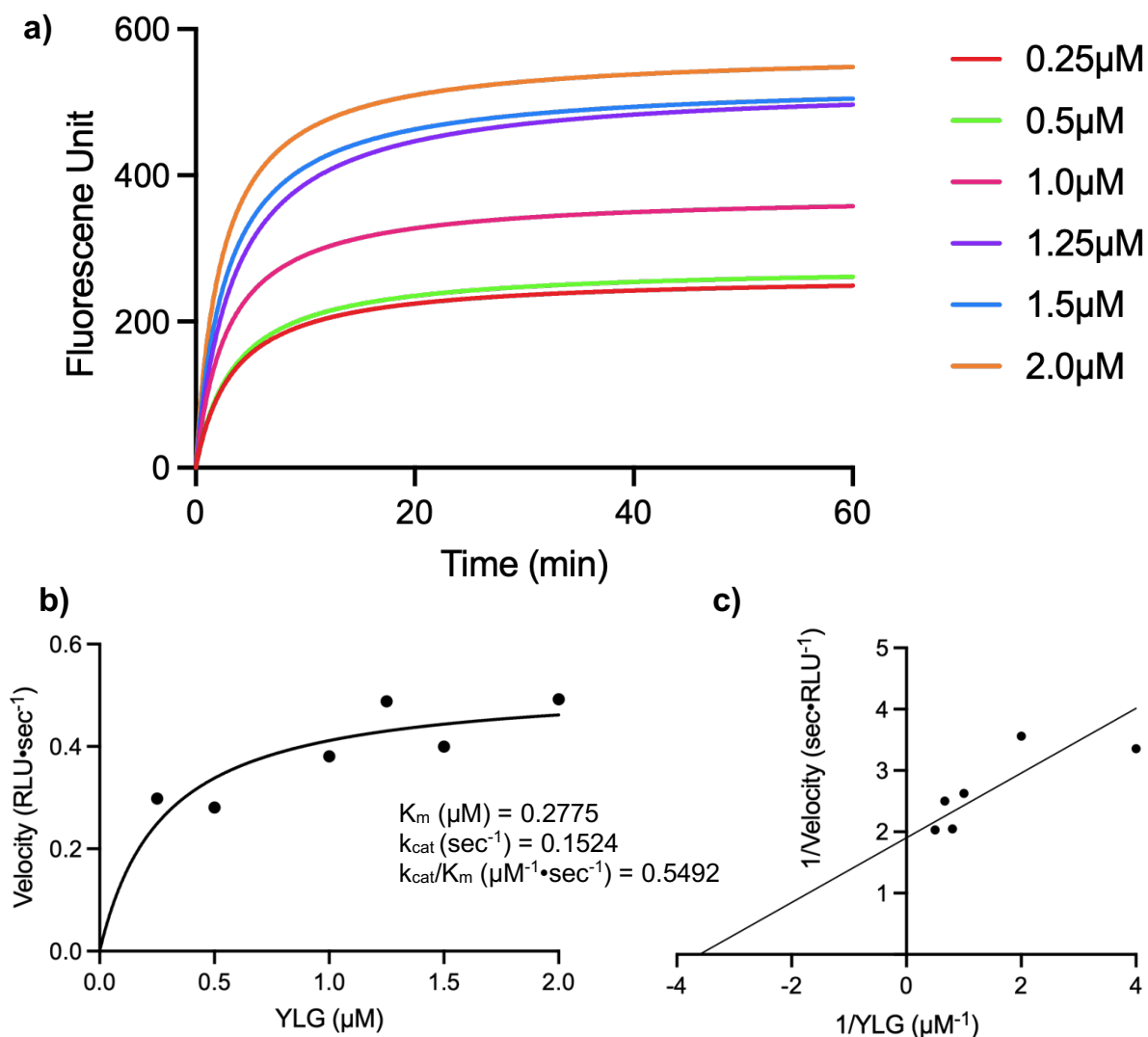

Figure 6: Kinetics of YLG hydrolysis by RMS3. **a)** The kinetics of RMS3 when subjected to increasing concentrations of YLG, monitored by fluorescence. **b)** RMS3 pre-steady-state kinetics reaction velocity with YLG, as shown in **a)**. **c)** Enzyme kinetics of RMS3 from **b)** shown as a Lineweaver-Burk plot. RLU = relative light unit.

Strigolactone-mediated formation of the RMS3-*Ps*MAX2 complex

An important aim of SL signaling research is to solve the structure of what is purported to be the signaling complex in its entirety; that is, an SL receptor-F-box-transcriptional repressor complex. In pea, RMS3 is the SL receptor, *Ps*MAX2 is the aforementioned F-box protein that acts as a substrate recognition unit, and *Ps*SMXL6, *Ps*SMXL7, and *Ps*SMXL8 are known transcriptional repressors that are recognized by MAX2 and targeted for ubiquitination and degradation.[28,29,39] Toward that end, we first demonstrated that RMS3 forms an SL-dependent complex with *Ps*MAX2 via SEC (**Fig. 7**), as has been previously shown for other SL receptors.[31]

*Ps*MAX2 was cloned, expressed, and co-purified with ASK1 (its partner in the SCF ubiquitin ligase complex that is integral for production of soluble MAX2) from insect cells (see **Methods** and Shabek 2018[31]). Two TEV sites were introduced between residues 436 and 504 to post-translationally eliminate a long, disordered loop via TEV cleavage. Post-cleavage, two *Ps*MAX2 fragments are generated that complex together, but are seen as separate bands when visualized by SDS-PAGE (denoted as MAX2i and MAX2ii in **Fig**. **7a** and **b**).

Purified ASK1-*Ps*MAX2 was combined with purified RMS3 in the presence or absence of (±)-GR24, incubated, and analyzed via SEC and SDS-PAGE. As expected, RMS3 co-eluted with *Ps*MAX2 to a far higher degree after having been incubated with (±)-GR24 (**Fig. 7b**), confirming that the presence of SL is integral for SL signaling complex formation in *P. sativum.*
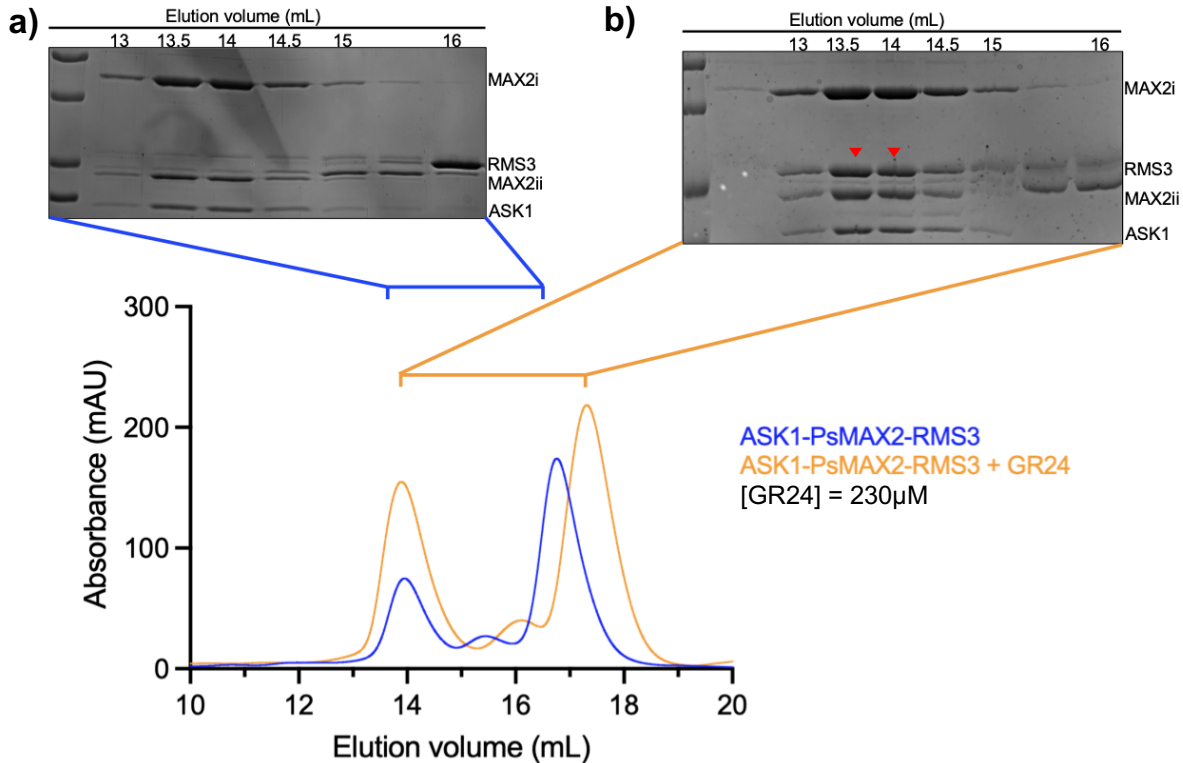
Figure 7: Size-exclusion chromatography analysis of the interaction between ASK1-*Ps*MAX2 and RMS3 in the presence or absence of (±)-GR24. Acetone was used in place of (±)-GR24 for **a).**

A critical next step is to express and purify all *Ps*SMXLs and recapitulate this experiment with the expectation that the three interactors will co-complex in a GR24-dependent manner. Determining the molecular structure of the signaling complex in its entirety will elucidate many questions regarding SL signaling mechanisms, specifically in pea. The benefits of this knowledge would extend to SL signaling in other organisms as well.

Structural examination of RMS3

To look more closely at the mechanisms of SL perception in pea, we crystallized and determined the structure of apo-RMS3 at 2.6Å resolution. The overall structure of RMS3 shows the typical α/β-fold hydrolase structure of a lid, base, and hydrophobic pocket (**Fig. 8b, d** and **Table 1**).
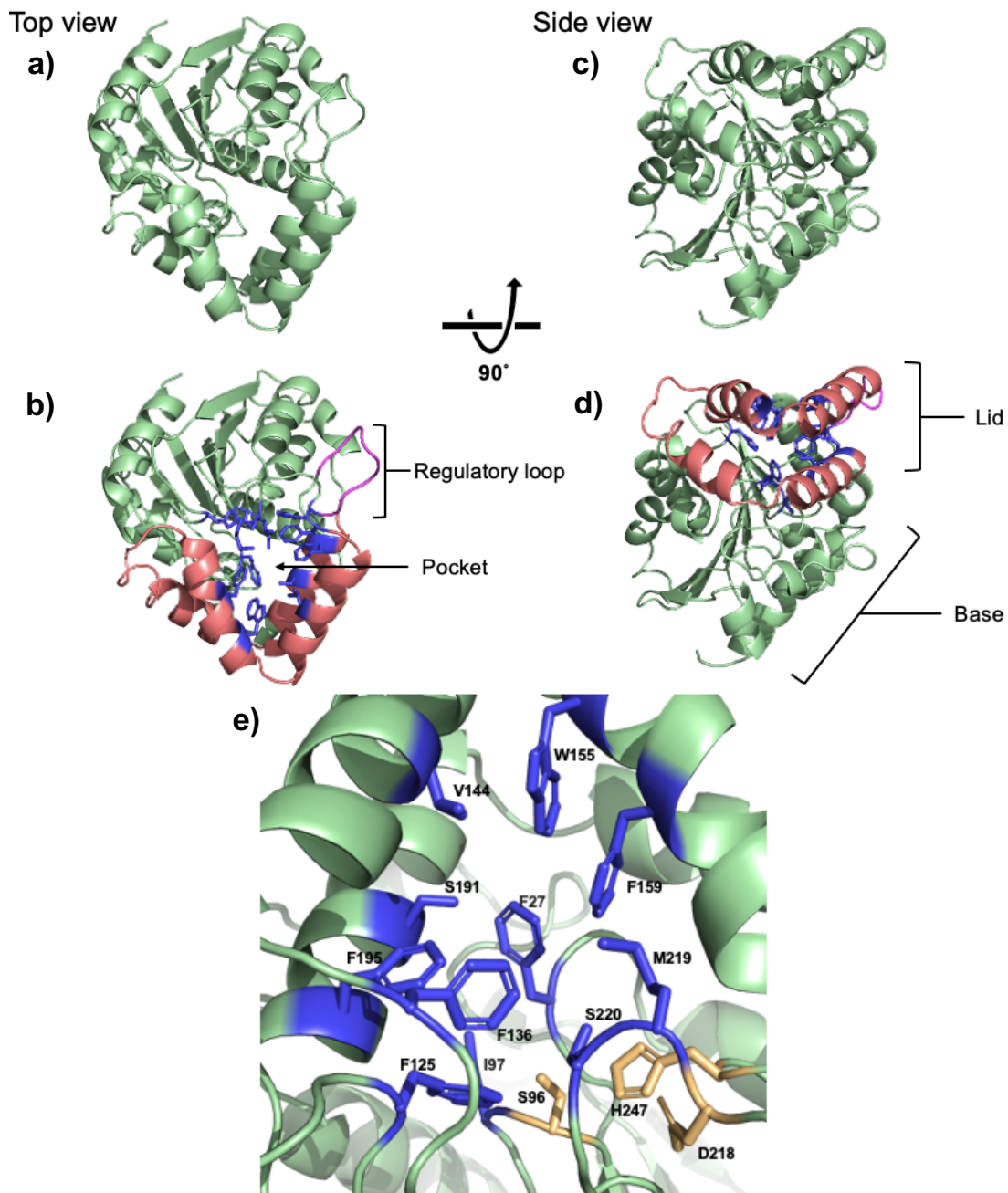
Figure 8: Structure of RMS3. **a)** and **c)** are top and side view representations of the RMS3 structure. **b)** and **d)** highlight key features: the base (pale green), lid (pale red), hydrophobic pocket (blue), and regulatory loop (magenta). **e)** denotes the residues that have hydrophobic interactions when a ligand is in the pocket (blue), as well as the catalytic Ser-His-Asp triad (pale orange).

Table 1: Data collection and refinement statistics.

	RMS3
Data collection	
Space group	P 6_1
Cell dimensions	
a, b, c (Å)	70.604, 70.604, 201.136
α, β, γ (°)	90, 90, 120
Resolution (Å)	45.18-2.601 (2.694-2.601)
R_{sym}	0.076 (1.160)
$I / \sigma I$	14.9 (1.7)
Completeness (%)	99.93 (99.88)
Redundancy	5.7(5.2)
Refinement	
Resolution (Å)	2.601
No. reflections	17383
R_{work} / R_{free} (%)	21.6/27.2
No. atoms	4305
Protein	4222
Ligand/ion	51
Water	32
B-factors	22.56
Protein	22.46
Ligand/ion	32.72
Water	19.91
r.m.s. deviations	
Bond lengths (Å)	0.003
Bond angles (°)	0.57

Solving the RMS3 atomic structure allowed us to further investigate the differences between SL perception in pea, the rest of the Fabaceae family to which pea belongs, and other plant families. To that end, we aligned 28 sequences from several plant families and sought out sequence divergences in key areas of the sequence, such as the hydrophobic pocket and the putative interface with D3/MAX2 that has previously been suggested for other SL receptors.[30,33] We identified two key differences that distinguish the structure of RMS3 and other members of the Fabaceae from other SL receptors in the plant kingdom. RMS3 has an isoleucine at position 97 (**Fig. 9a**)—a trait shared with all other members of the Fabaceae included this analysis—and a methionine at position 219 (**Fig. 9b**), also shared with most other Fabaceae sequences analyzed herein.
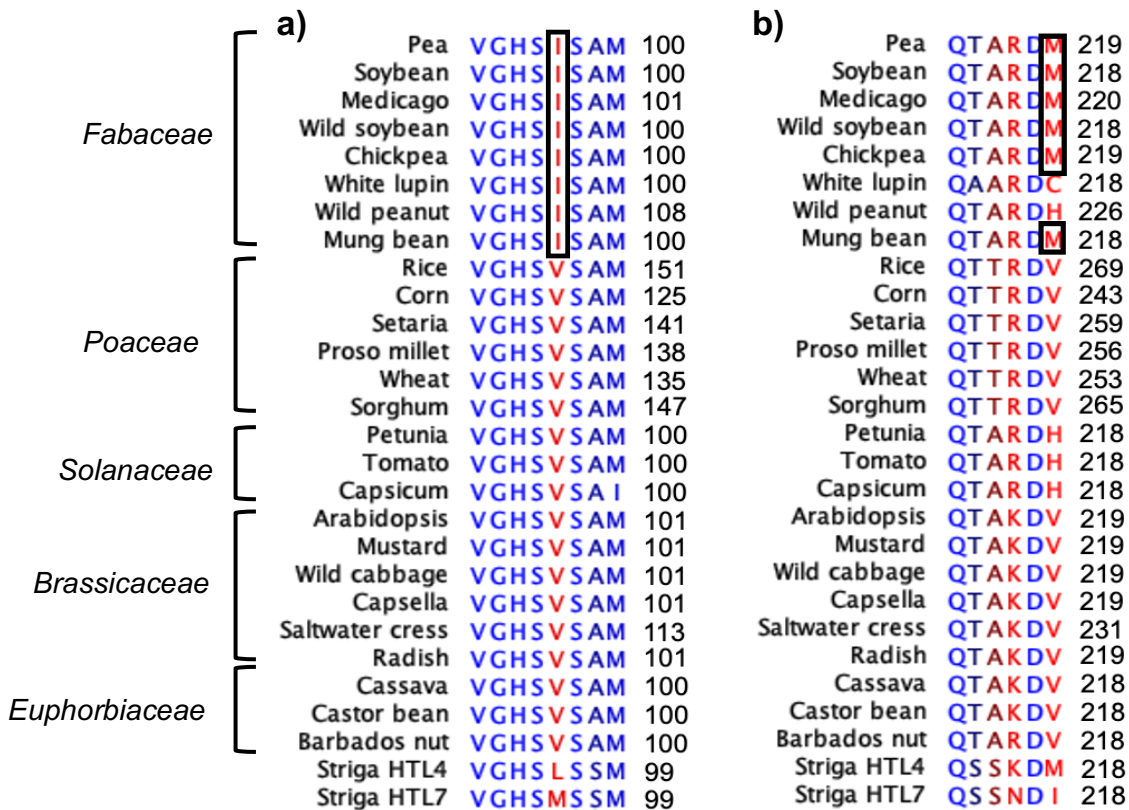

Figure 9: Sequence alignment of SL receptors. Highly conserved residues are colored in blue. The residues of interest (Ile97 and Met219 in pea) are within the black boxes. The labels to the left of the alignments indicate the plant families from which the species derive.

However, Ile97 is replaced with a valine in every other lineage (aside from *Striga*), and Met219 is most commonly substituted by a valine as well. These two amino acid positions were previously shown to be a part of the solvent-exposed hydrophobic pocket of rice D14.[30] We wondered if this Fabaceae-specific change in residue had an observable effect on the structure of RMS3 compared to other lineages of SL receptor. To that end, we aligned and compared our structure of RMS3 to a computationally-generated RMS3 model structure with I97V and M219V substitutions (**Fig. 10a** and **b**).
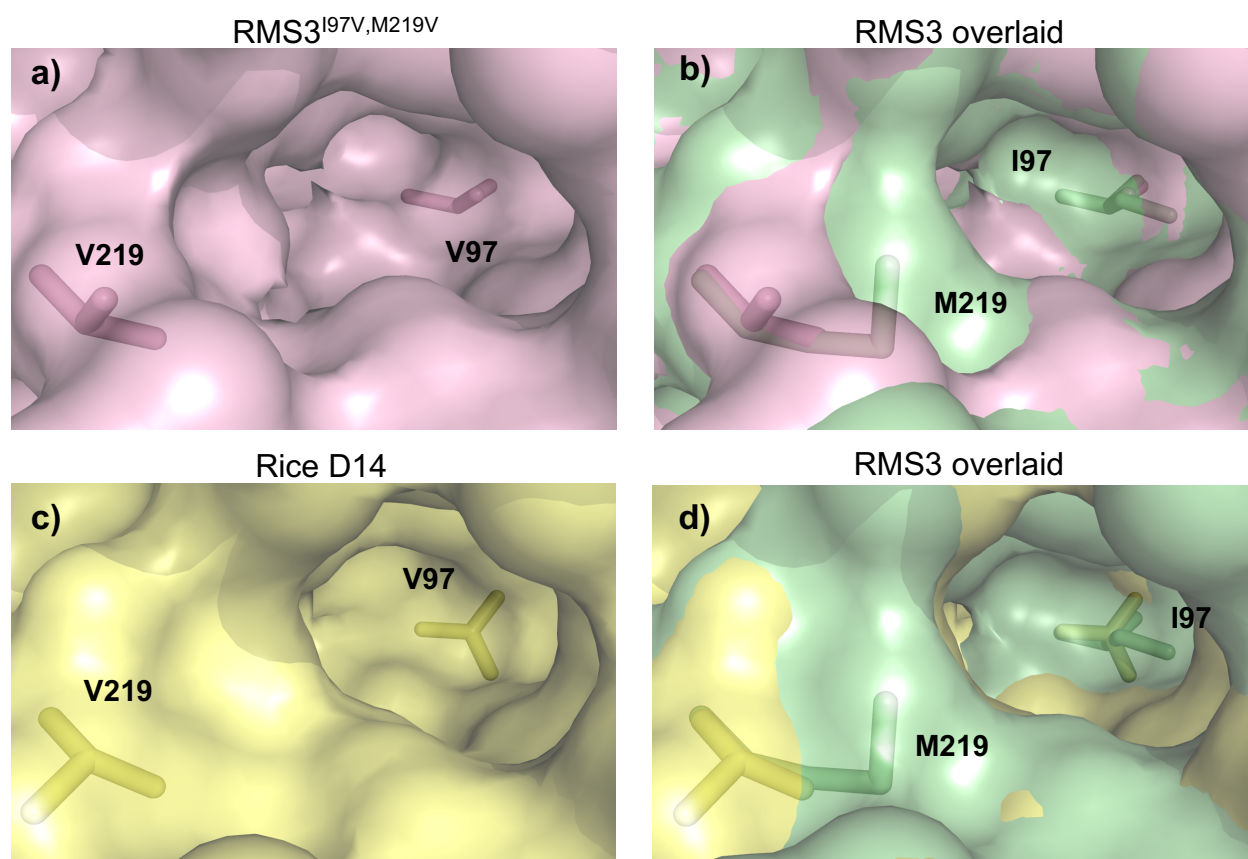

Figure 10: SL-binding pocket structures of **a)** RMS3[I97V, M219V0], **b)** RMS3[I97V, M219V0] aligned to wild-type RMS3, **c)** rice D14, and **d)** rice D14 aligned to wild-type RMS3. The surface of each protein has a transparency of 30%. The side chains of labeled residues are visible in stick representation.

There is an observable change in pocket size if these two residues are altered. Specifically, wild-type RMS3 appears to have a smaller pocket than RMS3[I97V, M219V] (**Fig. 10b**) due in part to the difference in residues at those specific positions. To further confirm

the role that Met219 and Ile97 have with regards to pocket size, we compared rice D14 (PBD: 3WIO)[23] to RMS3 (**Fig. 10c** and **d**). The structure for rice D14 is well-characterized and possesses valines at both residue positions in question. Notably, when RMS3 is aligned with the rice structure, the pocket is once again smaller.

To accurately compute the potential difference in pocket size between wild-type RMS3 and RMS3[I97V, M219V], we utilized the Computed Atlas of Surface Topography of proteins (CASTp),[40] a computational tool that calculates the Richards' solvent-accessible volume[41] of protein pockets. The pocket volume of RMS3[I97V, M219V] was calculated to be 115.278Å^3, while wild-type RMS3 possesses a pocket volume of 97.82Å^3. Thus, it appears that Ile97 and Met219 play an integral role in the pocket size of not only RMS3, but potentially other members of the Fabaceae as well. This difference in pocket size compared to other families of SL receptors could have implications for ligand specificity and/or enzymatic mode of action that should be further investigated in the future.[20,42] Exploring differences in pocket architecture is of vital importance considering the existence of more than 20 distinct SL ligands[43] that could potentially have variable effects on plant physiology.[4,21,42]

Mutagenesis of RMS3

Serine hydrolase enzymes utilize a catalytic triad by which the nucleophilic serine is activated by a proton relay consisting of the serine, an acidic residue, and a basic residue (aspartic acid and histidine in the case of SL receptors, respectively).[13,32] The serine then attacks and hydrolyzes the ligand (**Fig 11a**). To further clarify the hydrolysis mechanism of RMS3, we focused on the serine catalytic site. We designed two distinct RMS3 catalytic mutants using site-directed mutagenesis: (1) RMS3[S96A], where the catalytic Ser96 has

been mutated to an alanine; this mutant will be completely inactive due to the lack of nucleophilicity of alanine to attack SLs, and (2) RMS3[H247Y], where the catalytic His247 has been mutated to a tyrosine. While the properties of RMS3[H247Y] are unknown, we hypothesized that mutating His247 to tyrosine will provide an additional carbonyl group that could generate a transient tyrosine-serine relay and potentially mimic bound SL post-hydrolysis intermediate (**Fig. 11b** and **c**). The mutants were expressed and purified as described for RMS3 (**Figs. 12** and **13**).
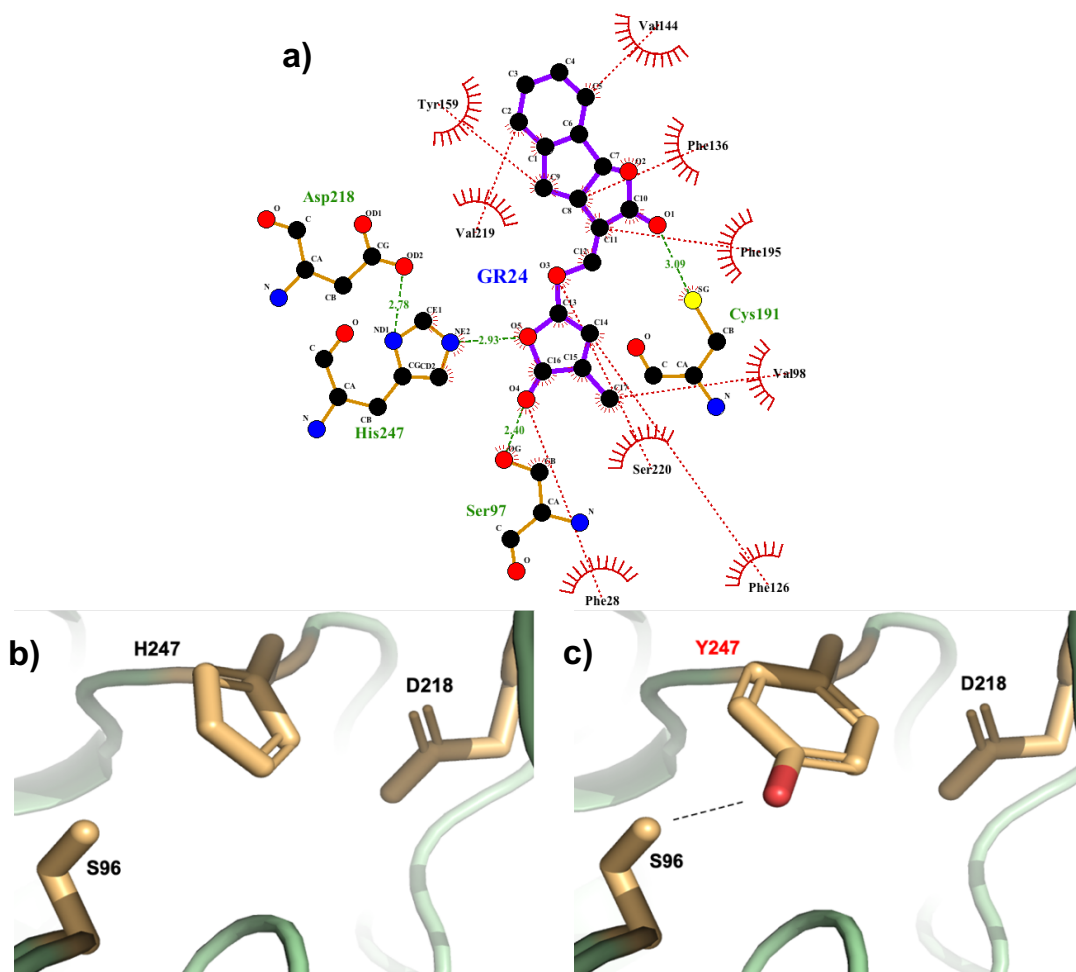

Figure 11: **a)** a LIGPLOT of the SL-binding pocket computed from a rice D14 structure (PDB: 5DJ5)[30] that was co-crystallized with GR24. The catalytic Asp, His, and Ser are visible on the left in ball-and-stick form. **b)** The catalytic Ser-His-Asp triad as seen in RMS3. **c)** A hypothetical depiction of the catalytic triad with a His247 to Tyr247 mutation. The dotted lines indicate a theorized interaction between Tyr247 and Ser96.
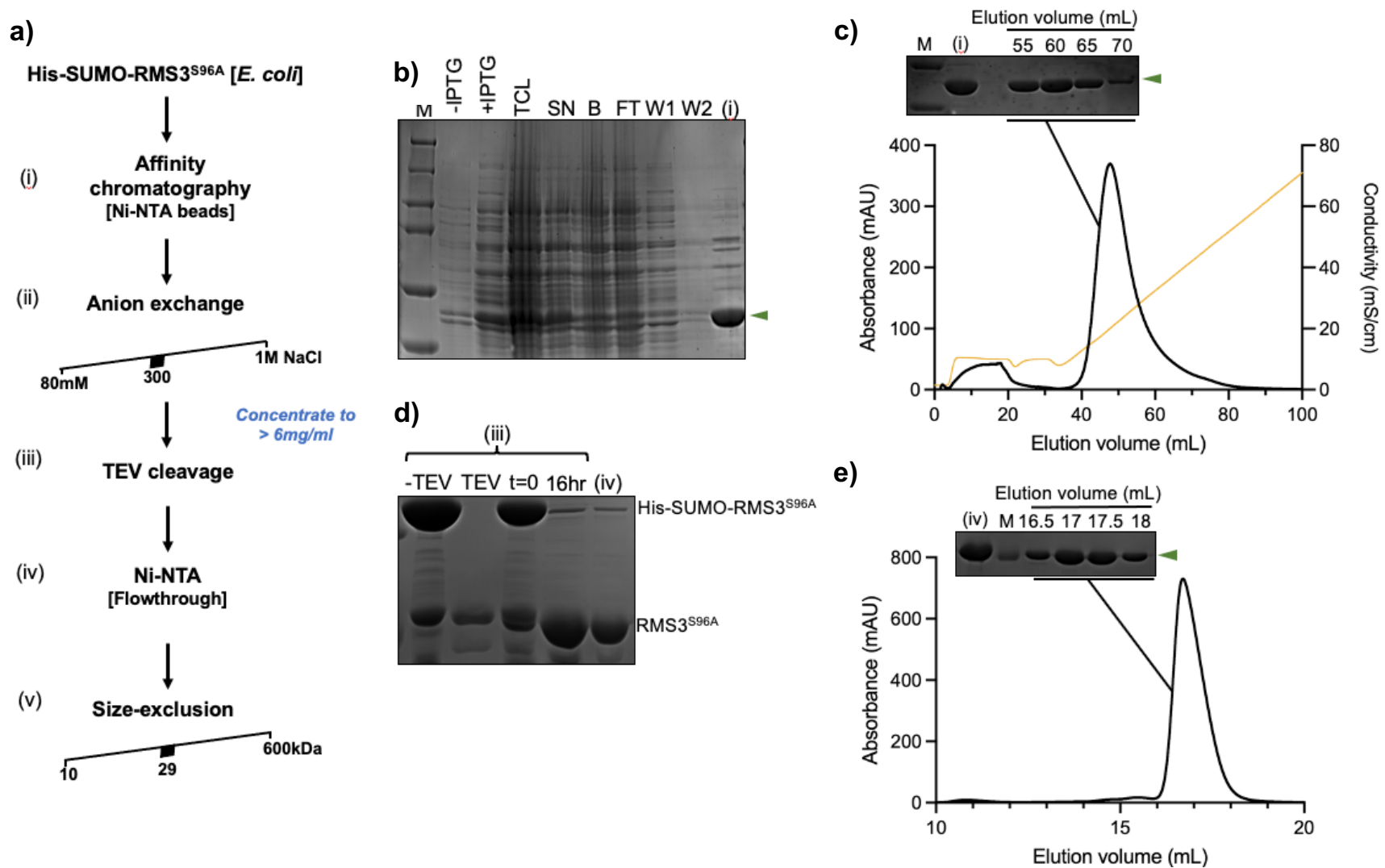
Figure 12: Purification of RMS3^{S96A}. a) The purification of RMS3^{S96A} laid out step by step, from expression in *E. coli* to tag cleavage and purification via size-exclusion chromatography. **b)** and **d)** Sodium dodecyl-sulfate polyacrylamide gels depicting different steps of the purification. M = marker, TCL = total cell lysate, SN = supernatant, B = beads post-binding, FT = flowthrough, W1 and W2 = wash 1 and wash 2 respectively. TEV = tobacco etch virus. **c)** Anion exchange chromatography of His-SUMO-RMS3^{S96A} and **e)** size-exclusion chromatography of RMS3^{S96A}, with sodium dodecyl sulfate-polyacrylamide gel electrophoresis analysis of the elution fractions.
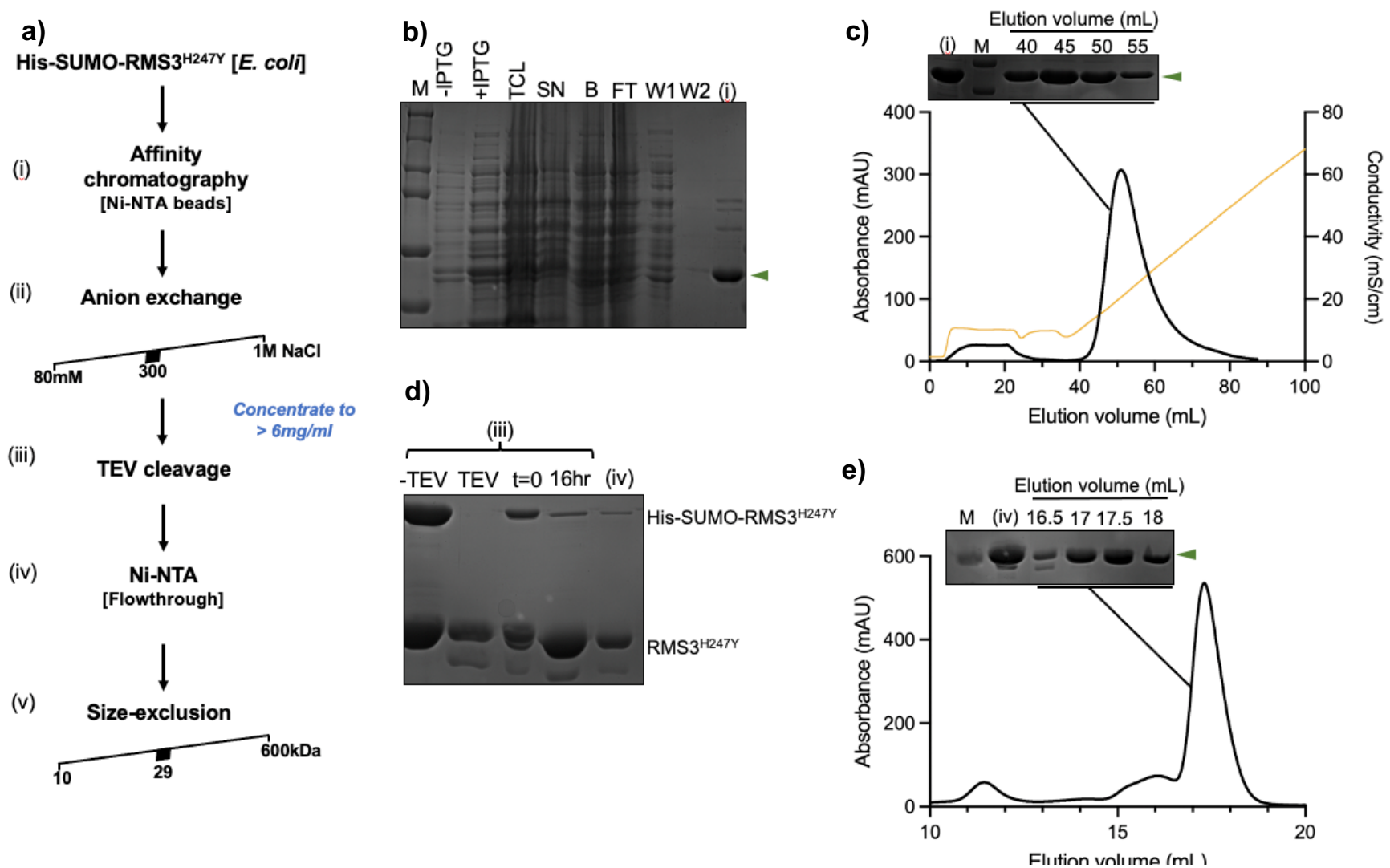
Figure 13: Purification of RMS3^{H247Y}. a) The purification of RMS3^{H247Y} laid out step by step, from expression in *E. coli* to tag cleavage and purification via size-exclusion chromatography. **b)** and **d)** Sodium dodecyl-sulfate polyacrylamide gels depicting different steps of the purification. M = marker, TCL = total cell lysate, SN = supernatant, B = beads post-binding, FT = flowthrough, W1 and W2 = wash 1 and wash 2 respectively. TEV = tobacco etch virus. **c)** Anion exchange chromatography of His-SUMO-RMS3^{H247Y} and **e)** size-exclusion chromatography of RMS3^{H247Y}, with sodium dodecyl sulfate-polyacrylamide gel electrophoresis analysis of the elution fractions.

Verification of RMS3^{S96A} and RMS3^{H247Y} activity via DSF

To confirm that RMS3^{S96A} was catalytically non-functional, we analyzed its response to a high concentration of (±)-GR24 using DSF (**Fig. 14a**). The starting T_m of approximately 44°C was slightly lower than the T_m of ~45.5°C seen in wild-type RMS3 (**Fig. 5**). Surprisingly, a slight increase in T_m was observed in response to the addition of (±)-GR24. To further unravel this phenomenon, we subjected RMS3^{S96A} to a gradient of (±)-GR24 and observed the same slight increase in T_m as a response to an increasing concentration of ligand (**Fig. 14b**).

The same experiments were carried out for RMS3^{H247Y}. Interestingly, we found an even lower starting T_m of 41-42°C, and an increase in T_m of several degrees upon the application of ligand (**Fig. 14c** and **d**).
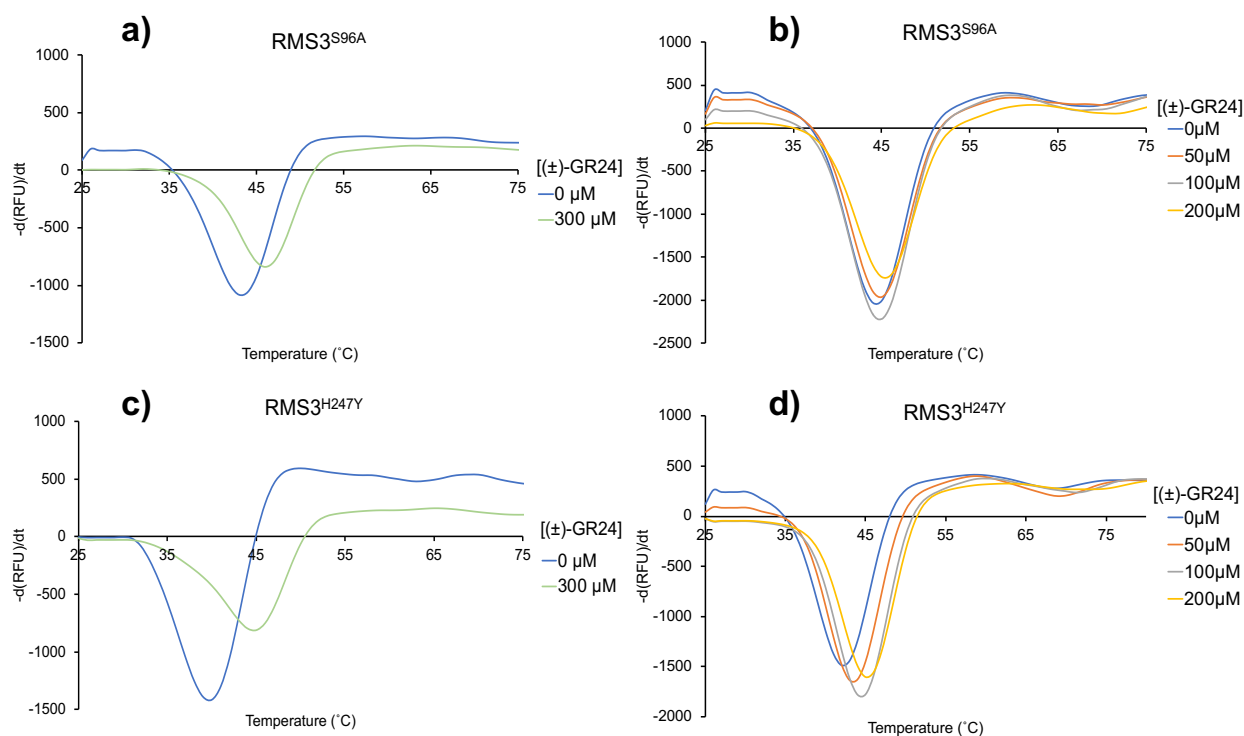

Figure 14: Melting temperature curves for **a)** and **b)** RMS3^{S96A} and **c)** and **d)** RMS3^{H247Y} at indicated concentrations of (±)-GR24, as assessed by DSF. Each line represents the average protein melt curve for three replicate samples run in parallel.

It is worth noting that the RMS3^{H247Y} T$_m$ of approximately 41°C without (±)-GR24 is the same as the T$_m$ of wild-type RMS3 when subjected to concentrations of ligand greater than 200μM, as seen in Figure 5. One possible explanation is that the H247Y mutation destabilizes the enzyme in a manner similar to the effect that has been previously shown for D14-SL post-hydrolysis conformational alteration.[13,30] As for the slight increase in T$_m$ in response to increasing concentrations of ligand seen in both RMS3^{S96A} and RMS3^{H247Y} (as opposed to the T$_m$ *decrease* in wild-type RMS3 seen with increasing concentrations of ligand), we postulate that this response may be due to the (±)-GR24 binding in the hydrophobic pocket without being hydrolyzed and thus causing a conformational shift that results in a slight increase in protein stability.

Analysis of RMS3^{S96A} and RMS3^{H247Y} hydrolytic activity via YLG hydrolysis

In an effort to further compare the catalytic mutants to wild-type RMS3 and to confirm a lack of hydrolytic activity, both mutants and wild-type were held at a constant concentration in the presence of YLG and analyzed (**Fig. 15**).
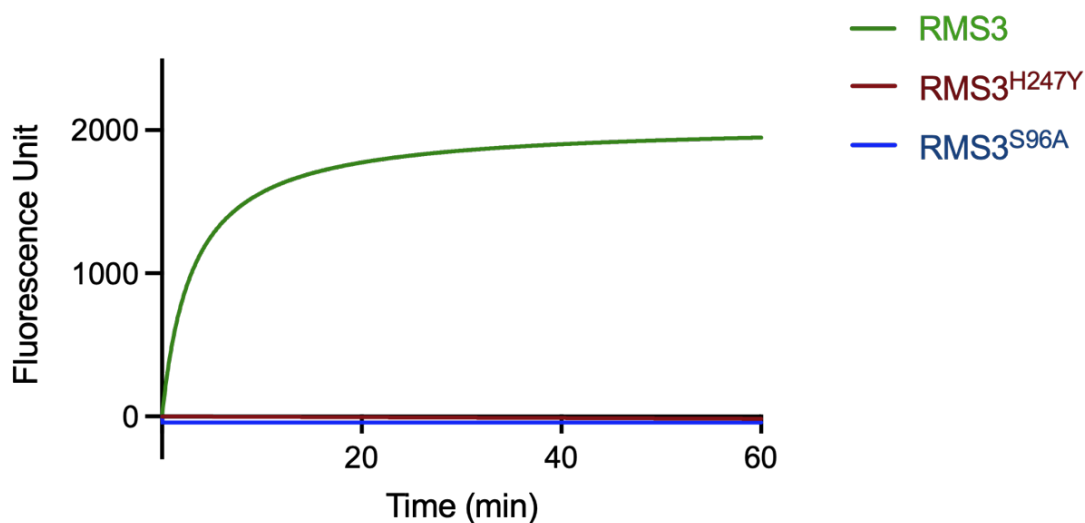

Figure 15: Kinetics of YLG hydrolysis by RMS3 (green), RMS3^{H247Y} (dark red), and RMS3^{S96A} (blue). Each curve represents an average of three identical samples run in parallel.

There was a total lack of hydrolytic activity in response to YLG, confirming that both

RMS3^{H247Y} and RMS3^{S96A} are catalytically inactive and are thus unable to hydrolyze

SLs.

<u>RMS3^{H247Y} does not interact with *Ps*MAX2 in the presence of SLs</u>

Because of the intrinsic instability and loss of catalytic activity, our data suggest that

RMS3^{H247Y} mimics an RMS3-SL post-hydrolysis state. Thus far, it has been unclear

whether the MAX2-RMS3-SL signaling complex is assembled before, during, or post-

hydrolysis of SL. To address this, we studied the ability of RMS3^{H247Y} to form a complex

with *Ps*MAX2 with or without the presence of (±)-GR24. As described for wild-type RMS3,

we similarly subjected RMS3^{H247Y} to SEC with *Ps*MAX2 (**Fig. 16)**. Interestingly, there is

little to no complex formation in the absence or the presence of (±)-GR24 (**Fig. 16a** and

b). This led us to conclude that the conformational changes of RMS3^{H247Y} that are likely

to mimic RMS3-SL post-hydrolysis state are either not sufficient to produce structural

changes in the enzyme that are necessary to create the appropriate interface for

*Ps*MAX2, and/or that the *Ps*MAX2-RMS3-SL complex is assembled before or during SL
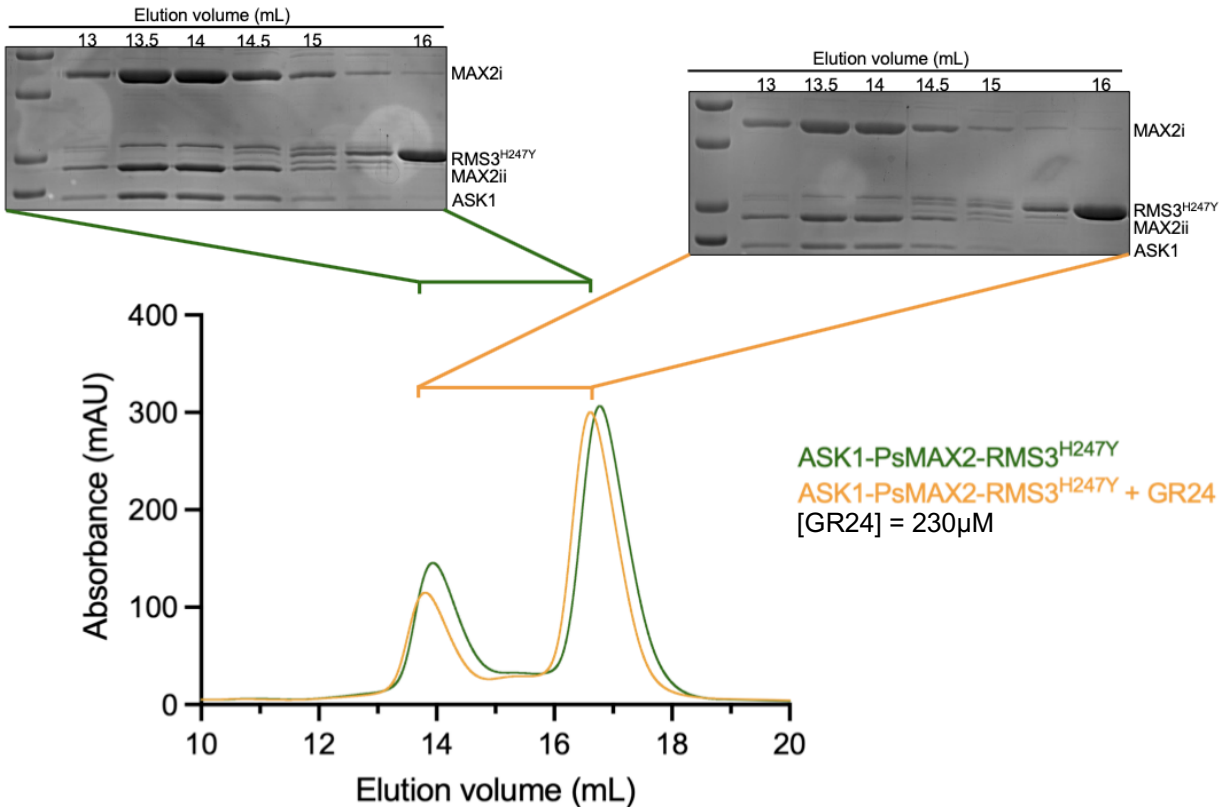
hydrolysis rather than after.

Figure 16: Size-exclusion chromatography analysis of the interaction between ASK1-*Ps*MAX2 and RMS3^{H247Y} in the presence or absence of (±)-GR24. Acetone was used in place of (±)-GR24 for **a).**

Future directions

In this work we determined the crystal structure of RMS3 and provide detailed biochemical analysis into SL perception and hydrolysis. We further address a fundamental question regarding the process of RMS3-SL recruitment by MAX2 ubiquitin ligase and suggest that the timing of SL hydrolysis plays a role in complex assembly. Despite the advances of this work, SL signaling in pea remains to be fully resolved. Towards that goal, it would be interesting to solve the crystal structure of RMS3 with a ligand present, which would provide a clearer view as to how exactly SLs interact with the pocket of RMS3. It is even more imperative to produce full-length *Ps*SMXLs in order to

fully elucidate the entire signaling complex, and further reveal its structure and function *in vitro* and ultimately *in planta*. Given our results, it would also be interesting to determine the atomic structure of RMS3[H247Y], which would shed light on the effects and structural impact of the His247 to Tyr247 mutation. Last, based on our sequence and structural conservation analysis, it would be important to study the activity and ligand-binding specificity of RMS3 by substitution of Ile97 and Met219 to valines, which most other SL receptors have.

In summary, the data uncovered in this work hold the potential to broadly impact research into SL perception and signaling in legumes and beyond. What we have elucidated could potentially guide future studies into the mechanism of SL perception and signal propagation and possibly serve as an inroad for synthetic biology applications of SL research.

Methods

<u>Molecular cloning</u>

RMS3 was cloned and expressed as a 6×His-SUMO fusion protein from the expression vector pAL (Addgene) using the Ligation Independent Cloning (LIC) system. RMS3[S96A] and RMS3[H247] were generated by site-directed mutagenesis experiments performed on pAL-RMS3. Mutagenesis was verified by systematic DNA sequencing. All primers are listed in **Table 2**.

Table 2: Primers used for cloning of RMS3 and RMS3 mutants.

Name:	Sequence:
RMS3_F	5'-aaaacctctacttccaatcgATGGGCACTCCCATCCTC-3'
RMS3_R	5'-ccacactcatcctccggCTACTGCGAAAGTGCAATCTC-3'
RMS3[S96A]_F	5'-TGTGCTTACGTAGGTCACGCCATCTCCGCCATGACCG-3'
RMS3[S96A]_R	5'-CGGTCATGGCGGAGATGGCGTGACCTACGTAAGCACA-3'
RMS3[H247]_F	5'-GTGGCTTGACACGGAGGGGTATCTTCCTCATTTGAGTGC-3'

RMS3[H247]_R	5'-GCACTCAAATGAGGAAGATACCCCTCCGTGTCAAGCCAC-3'

Small scale expression test

The His-SUMO-RMS3 plasmid was transformed into BL21 (DE3) and selected on LB agar plates containing 25µg/mL chloramphenicol. After growing overnight at 37˚C, a single colony was selected and used to inoculate 5mL LB containing 25µg/mL chloramphenicol in a 14mL polypropylene culture tube (Fisher) and grown overnight at 37˚C. 80uL of this starter culture was then used to inoculate fresh 5ml LB with 25µg/mL in a 14ml polypropylene tube. This culture was shaken at 225rpm at 37˚C until OD_{600} reached ~0.7. 500uL of this – considered the "pre-induction" sample – was decanted into an Eppendorf tube and centrifuged at 14,000rpm for 30 seconds. After decanting the supernatant, the pellet was resuspended in Laemmli sample buffer and prepared for visualization via SDS-PAGE. 0.3mM IPTG was used to induce protein expression in the remaining culture which was then shaken at 37C for 4-5hrs. 200uL of this was decanted into an Eppendorf tube and centrifuged at 14,000rpm for 30 seconds. The pellet was resuspended in Laemmli sample buffer and visualized via SDS-PAGE alongside the pre-induction sample (**Fig. 3**).

Protein purification

The full-length pea MAX2 (*P. sativum*) and *A. thaliana* ASK1 were co-expressed as a 6 × His–2 × Msb (msyB)[44] fusion protein and an untagged protein, respectively, in Hi5 suspension insect cells. The ASK1–*Ps*MAX2 complex was isolated from the soluble cell

lysate by Q Sepharose High Performance resin (GE Healthcare). NaCl eluates (500 mM) were subjected to Nickel Sepharose Fast Flow resin (GE Healthcare) and were eluted with 250 mM imidazole. To remove the 6 × His–2 × Msb fusion tag, the clarified complex was cleaved at 4 °C for 16hr by tobacco etch virus (TEV) protease and was further purified by anion exchange. For crystallization and biochemical analysis purposes, the *Ps*MAX2-expressing construct was designed to eliminate a non-conserved 67-residue disordered loop between residue 436 and residue 504 after affinity purification. The resulting *Ps*MAX2 fusion protein contains a 6× His–2 × Msb tag at the N terminus and three TEV protease sites: between the Msb tag and *Ps*MAX2, after E436, and before G504, yielding a purified split form of *Ps*MAX2 with *Ps*MAX2 N-terminal domain (1–436) and C-terminal domain (504-707) stably associated (see **Fig. 7**).

For all RMS3s, BL21 (DE3) cells transformed with the expression plasmid were grown in LB broth at 16 °C to an OD_{600} of ~0.7 and induced with 0.3mM IPTG for 16hr. Cells were harvested by centrifugation at 4,000rpm for 20min at 4°C (Beckman Avanti JXN-26), re-suspended and lysed in lysis buffer (50mM Tris-HCl, pH 8.0, 250mM NaCl, 5mM imidazole). The lysate was centrifuged at 19,000rpm for 1hr at 4°C (Beckman Avanti J-25I). The supernatant was loaded onto a disposable polypropylene column packed with HisPur Ni-NTA Superflow Agarose resin (Thermofisher). The column was washed copiously, first with a buffer composed of 50mM Tris-HCl, pH 8.0, 500mM NaCl, and 10mM imidazole, then with a second buffer composed of 50mM Tris-HCl, pH 8.0, and 10mM imidazole. The His-SUMO-RMS3s were then eluted with 300mM imidazole and loaded onto a HiTrap Q FF Anion Exchange column (5mL, GE Healthcare, Åkta Pure system) and subjected to anion-exchange. The purity of the eluted fractions was resolved

by 13% SDS-PAGE and visualized via Coomassie blue stain. The fractions were then concentrated to 6mg/mL or greater and cleaved with TEV protease overnight at 4 °C. The cleaved His-SUMO tag was removed by passing through Ni-NTA resin. All RMS3s were further purified by size-exclusion chromatography through a Superdex-200 gel filtration column (GE Healthcare, Åkta Pure system) in 20mM HEPES, pH 7.3, 150mM NaCl, 5mM DTT and 1% glycerol. The purity of the elution fractions was resolved by 13% SDS-PAGE and visualized by Coomassie blue stain. All proteins were then concentrated to 3–12 mg/mL and flash frozen in liquid nitrogen before being stored at -80˚C until use.

Differential scanning fluorimetry

DSF experiments were performed on a CFX96 Touch^{TM} Real-Time PCR Detection System (Bio-Rad Laboratories, Inc., Hercules, California, USA) using excitation and emission wavelengths of 490 and 575nm, respectively. Sypro Orange ($\lambda_{ex}/\lambda_{em}$: 470/570nm; Life Technologies Co., Carlsbad, California, USA) was used as the reporter dye. Samples were heat-denatured using a linear 25 to 95°C gradient at a rate of 1.3°C per minute. Plates were incubated in darkness on ice for 30min before analysis. The denaturation curve was obtained using CFX manager™ software. Final reaction mixtures were prepared in triplicate in 96 well white microplates, and each reaction was carried out in 30µL scale in Superdex-200 buffer (20mM HEPES, pH 7.3, 150mM NaCl, 5mM DTT, 1% Glycerol) containing 20uM protein, 0-300µM (±)-GR24 (as shown in **Fig. 5b**), and 0.075µL Sypro Orange. In the control reaction, an equal volume of acetone was added instead of ligand. The experiments were repeated at least three times.

Crystallization, data collection and structure determination

The crystals of RMS3 were grown at 4°C by the hanging-drop vapor diffusion method with 1.0uL purified protein sample mixed with an equal volume of reservoir solution containing 0.1M MES/imidazole pH 6.5, 12.5% w/v PEG 1000, 12.5% w/v PEG 3350, 12.5% v/v MPD and 0.3M each of sodium nitrate, disodium hydrogen phosphate, and ammonium sulfate. Crystals of maximum size were obtained and harvested after one week from the reservoir solution. X-ray diffraction data was integrated and scaled with HKL2000 package.[45] RMS3 crystal structures were determined by molecular replacement using an *At*D14 model (PDB: 4IH9)[34] as the search model. All structural models were manually built, refined, and rebuilt with PHENIX[46] and COOT.[47] In PHENIX, the *At*D14 structure was transformed into a polyalanine model, onto which the amino acid sequence of RMS3 was sculpted. The structure then underwent molecular replacement and was refined to a resolution of 2.6Å. All structural statistics can be seen in **Table 1**.

YLG hydrolysis assay

YLG (TCI America) hydrolysis assays were performed using 3.45µM of recombinant proteins in a reaction buffer (50mM MES pH 6.5, 150mM NaCl and 1mM DTT) at a 50µl volume on a 96-well black plate (Greiner). The fluorescence intensity was measured by a Synergy H1 microplate reader (BioTek) at excitation by 480nm and detection by 520nm. Time-course experiments were performed in 10s intervals over 60min. Data generated in Excel were transferred to Prism 9 for graphical analysis and curve-fitting.

Co-complexing via size-exclusion chromatography

Purified proteins (15-100µM) were incubated with 230µM (±)-GR24 (Chiralix), or equal volume of acetone as the solvent control, at 4°C for 30min in 20mM HEPES, pH 7.0,

150mM NaCl and 2mM DTT. The reaction was injected onto a Superdex-200 Increase 10/300 column (GE Healthcare) for analysis at a flow rate of 0.5ml min^{-1}. The elution fractions (0.5ml per fraction) were resolved by SDS–PAGE and analyzed by Coomassie blue stain.

Acknowledgments

References

1. Tal, Lior et al. Structural aspects of plant hormone signal perception and regulation by ubiquitin ligases. Plant Phys. 182(4),1537-1544 (2020).

2. Jaillais, Y., Chory, J. Unraveling the paradoxes of plant hormone signaling integration. Nat. Struct. Mol. Biol. 17, 642–645 (2010).

3. Kelley, D. R., Estelle, M. Ubiquitin-mediated control of plant hormone signaling. Plant Phys. 160(1), 47–55 (2012).

4. Marzec, M. Perception and signaling of strigolactones. Front. Plant Sci. 7, 1260 (2016).

5. Cook, C. E. et al. Germination of witchweed (Striga lutea Lour.): isolation and properties of a potent stimulant. Science 154(3753), 1189–1190 (1966).

6. Xie, X., Yoneyama, K., Yoneyama, K. The strigolactone story. Annu. Rev. Phytopathol. 48, 93–117 (2010).

7. Machin, D.C., Hamon-Josse, M., Bennett, T. Fellowship of the rings: a saga of strigolactones and other small signals. New Phytol. 225, 621-636 (2020).

8. Snowden, K.C. et al. The Decreased apical dominance1/Petunia hybrida CAROTENOID CLEAVAGE DIOXYGENASE8 gene affects branch production and plays a role in leaf senescence, root growth, and flower development. Plant Cell. 17, 746–759 (2005).

9. Yan, H., et al. Rice tillering dwarf mutant dwarf3 has increased leaf longevity during darkness-induced senescence or hydrogen peroxide-induced cell death. Genes Genet. Syst. 82, 361–366 (2007).

10. Shinohara, N., Taylor, C., Leyser, O. Strigolactone can promote or inhibit shoot branching by triggering rapid depletion of the auxin efflux protein PIN1 from the plasma membrane. PLoS Biol. 11, e1001474 (2013).

11. Gomez-Roldan, V., et al. Strigolactone inhibition of shoot branching. Nature 455(7210), 189–194 (2008).

12. Umehara, M. et al. Inhibition of shoot branching by new terpenoid plant hormones. Nature 455, 195–200 (2008).

13. Hamiaux, C. et al. DAD2 is an alpha/beta hydrolase likely to be involved in the perception of the plant branching hormone, strigolactone. Curr. Biol. 22, 2032–2036 (2012).

14. Soundappan, I. et al. SMAX1-LIKE/D53 family members enable distinct MAX2-dependent responses to strigolactones and karrikins in Arabidopsis. Plant Cell 27, 3143–3159 (2015).

15. Bu, Q.Y. et al. Regulation of drought tolerance by the F-box protein MAX2 in Arabidopsis. Plant Phys. 164, 424–439 (2014).

16. Ha, C.V. et al. Positive regulatory role of strigolactone in plant responses to drought and salt stress. Proc. Natl. Acad. Sci. USA 111, 851–856 (2014).

17. Yoneyama, K., Nitrogen deficiency as well as phosphorus deficiency in sorghum promotes the production and exudation of 5-deoxystrigol, the host recognition signal for arbuscular mycorrhizal fungi and root parasites. Planta 227(1), 125-132 (2007).

18. Jamil, M. et al. Quantification of the relationship between strigolactones and Striga hermonthica infection in rice under varying levels of nitrogen and phosphorus. Weed Res. 51, 373–385 (2011).

19. Zwanenburg, B., Pospíšil,T. Structure and activity of strigolactones: new plant hormones with a rich future. Mol. Plant 6(1), 38-62 (2013).

20. Wang, Y., Bouwmeester, H. J. Structural diversity in the strigolactones. J. Exp. Bot. 69(9), 2219–2230 (2018).

21. Yoneyama, K. et al. Strigolactones: structures and biological activities. Pest. Manag. Sci. 65(5), 467-70 (2009).

22. de Saint Germain, A. et al. Novel insights into strigolactone distribution and signalling. Curr. Opin. Plant Biol. 16, 583–589 (2013).

23. Nakamura, H. et al. Molecular mechanism of strigolactone perception by DWARF14. Nat. Commun. 4, 2613 (2013).

24. Zheng, N., Shabek, N. Ubiquitin ligases: structure, function, and regulation. Annu. Rev. Biochem. 86, 129-157 (2017).

25. Shabek, N., Zheng, N. Plant ubiquitin ligases as signaling hubs. Nat. Struct. Mol. Biol. 21(4), 293-296 (2014).

26. Arite, T. et al. D14, a strigolactone-insensitive mutant of rice, shows an accelerated outgrowth of tillers. Plant Cell Physiol. 50(8), 1416–1424 (2009).

27. Chevalier, F. et al. Strigolactone promotes degradation of DWARF14, an alpha/beta hydrolase essential for strigolactone signaling in Arabidopsis. Plant Cell 26, 1134–1150 (2014).

28. Jiang, L. et al. DWARF 53 acts as a repressor of strigolactone signalling in rice. Nature 504, 401–405 (2013).

29. Zhou, F. et al. D14-SCF(D3)-dependent degradation of D53 regulates strigolactone signalling. Nature 504, 406–410 (2013).

30. Zhao, L.H. et al. Destabilization of strigolactone receptor DWARF14 by binding of ligand and E3-ligase signaling effector DWARF3. Cell. Res. 25, 1219–1236 (2015).

31. Shabek, N. et al. Structural plasticity of D3–D14 ubiquitin ligase in strigolactone signalling. Nature 563, 652–656 (2018).

32. de Saint Germain, A. et al. An histidine covalent receptor and butenolide complex mediates strigolactone perception. Nat. Chem. Biol. 12, 787–794 (2016).

33. Yao, R. et al. DWARF14 is a non-canonical hormone receptor for strigolactone. Nature 536, 469–473 (2016).

34. Zhao, L.H. et al. Crystal structures of two phytohormone signal-transducing alpha/beta hydrolases: karrikin-signaling KAI2 and strigolactone-signaling DWARF14. Cell Res. 23, 436–439 (2013).

35. Kagiyama, M. et al. Structures of D14 and D14L in the strigolactone and karrikin signaling pathways. Genes Cells 18, 147–160 (2013).

36. Takeuchi, J. Rationally designed strigolactone analogs as antagonists of the D14 receptor. Plant Cell Physiol. 59(8), 1545–1554 (2018).

37. Lumba, S., Bunsick, M., McCourt, P. Chemical genetics and strigolactone perception. F1000Res. 6, 975 (2017).

38. Niesen, F., Berglund, H., Vedadi, M. The use of differential scanning fluorimetry to detect ligand interactions that promote protein stability. Nat. Protoc. 2, 2212–2221 (2007).

39. Wang, L. et al. Strigolactone signaling in Arabidopsis regulates shoot development by targeting D53-Like SMXL repressor proteins for ubiquitination and degradation. Plant Cell, 27(11), 3128–3142 (2015).

40. Tian, W. et al. CASTp 3.0: computed atlas of surface topography of proteins. Nucleic Acids Res. 46(W1), W363–W367 (2018).

41. Lee, B., Richards, F. M. The interpretation of protein structures: Estimation of static accessibility. J. Mol. Bio. 55(3), 379–IN4 (1971).

42. Flematti, G.R., et al. Stereospecificity in strigolactone biosynthesis and perception. Planta 243, 1361–1373 (2016).

43. Bürger, M. and Chory, J. In-silico analysis of the strigolactone ligand-receptor system. Plant Direct 4, e00263 (2020).

44. Su, Y., et al. The acidity ofprotein fusion partners predominantly determines the efficacy to improve the solubility of the target proteins expressed in Escherichia coli. J. Biotechnol. 129, 373–382 (2007).

45. Otwinowski, Z., Minor, W. Processing of X-ray diffraction data collected in oscillation mode. Methods Enzymol. 276, 307–326 (1997).

46. Adams, P. D. et al. PHENIX: A comprehensive Python-based system for macromolecular structure solution. Acta Crystallogr. Sect. D Biol. Crystallogr. 66, 213–221 (2010).

47. Emsley, P. et al. Features and development of Coot. Acta Crystallogr. Sect. D Biol. Crystallogr. 66, 486–501 (2010).